# On the mechanism of oxidation-fatigue damage at intermediate temperatures in a single crystal Ni-based superalloy

*A. Evangelou[1], K.A. Soady[2], S. Lockyer[2], N. Gao[1], P.A.S. Reed[1]*

1. Engineering Materials Research Group, Faculty of Engineering and Environment, University of Southampton, UK

2. Uniper Technologies Limited, Ratcliffe-on-Soar, Nottinghamshire, UK

Keywords: Crack tip, Intermediate temperature, Oxidation, Single crystal

## Abstract

The combined effects of environment (oxidation) and mechanical load (fatigue) that control crack propagation in a single crystal Ni-based superalloy have been investigated with particular focus on the intermediate service temperature range. Fatigue tests have been carried out at different frequencies, hold times and environments, to study the parameters influencing crack propagation at 550$^{o}$C. The direct current potential drop method was used to monitor the crack growth while STEM-EDS were used to analyse the fracture mode and crack tip regions.

It was found that the micro-mechanism of fatigue crack propagation at intermediate temperatures is a complex process with several competing mechanisms acting on the crack tip simultaneously. Crystallographic slip processes by γ' shearing are active at these temperatures while at the same time thermally activated processes that promote crack propagation through the γ channels also take place. In addition, the effects of oxidation were found to be two-fold. It was demonstrated that these temperatures are not high enough to cause macroscopic embrittlement of the crack tip but finger-like protrusions were found to penetrate the material ahead of the crack tip at the nano-scale. The kinetics of such a mechanism were accentuated by the plastic strains at the crack tip, which given enough time, can promote cleavage fracture at the γ/γ' interface. At the same time, given that the crack

driving force is lower than a transition value, oxide formation on the crack tip surfaces can bridge the opening of the crack tip and reduce the effective driving force.

# 1 Introduction

Single crystal Ni-based superalloys have long been the material of choice for gas turbine blade applications due to their excellent high temperature properties. Comprising the core of the gas turbine, the high cost of turbine blade replacement or refurbishment is a real incentive for the power generation industry to improve lifing approaches to allow for safe life extension as well as for optimising the life management. In order to accurately predict the remaining life, the detrimental, synergistic effects of environment and cyclic loading need to be fully understood. In addition, considering the complex shape of turbine blades and the significant temperature gradients, resulting from the incorporation of internal cooling passages and thermal barrier coatings, unpredictable failures can occur at a range of temperatures and therefore life prediction models should be developed to account for the associated damage. The main difficulty in doing so arises from the lack of a physical description of the interacting processes that take place at a crack tip during high temperature dwell fatigue. In many early attempts [1–4], the problem is approached by simply considering a linear summation of two independent damage mechanisms: oxide induced (time dependent) crack propagation and fatigue (cycle dependent) crack propagation i.e. $\frac{da}{dN}_{total} = \frac{da}{dN}_{fatigue} + \frac{da}{dN}_{oxidation}$. This approach however, fails to capture the synergistic phenomena that interact and simultaneously take place ahead of a propagating crack. This issue can be exacerbated at intermediate temperatures where neither of the two mechanisms (time or cycle dependent) dominates.

It is known that oxidation can reduce the effective crack driving force by wedging the crack tip due to the formation of thick oxides on the crack surfaces (oxidation induced closure) [5,6]. On the other hand, in other cases oxidation has been shown to act detrimentally to increase fatigue crack propagation. Stress assisted oxidation can lead to embrittlement and degradation of the mechanical properties in micro-volume in the material ahead of a crack tip [7,8]. Direct evidence of such an embrittled zone has been previously shown in CMSX-4 when the fatigue crack propagation (FCP)

rates of pre-oxidised and non-oxidised specimens have been compared [9]. At the nano-scale, the interaction of dislocations and oxidation was also shown to promote higher fatigue crack growth rates. Oxygen adsorbing on freshly emerging slip steps during fatigue inhibits the reversed slip mechanism and effectively results in larger, net slip irreversibility [10–12].

The majority of published work on the influence of oxidation on FCP in Ni-based superalloys is concerned with polycrystalline materials where the aforementioned mechanisms can be distinguished principally in terms of their effect on grain boundaries. Two mechanisms can be postulated to take place during dwell fatigue in single crystals: i) propagation by failure of an embrittled element ahead of the crack tip and ii) propagation by dynamic embrittlement and separation of the matrix-precipitate interface.

This paper aims to examine the damage mechanisms acting at a crack tip during fatigue in a single crystal Ni-based superalloy at intermediate service temperatures (550°C) and provide a physical interpretation of the damage process. Carefully designed mechanical tests have therefore been carried out at different frequencies, hold times and environments to obtain an understanding of the parameters influencing crack propagation. Scanning electron microscopy (SEM) was used to identify the fracture mode while scanning transmission electron microscopy (STEM) with high resolution energy dispersive spectroscopy (EDS) detectors was used to analyse crack tip regions.

# 2 Experimental Procedure

## 2.1 Material

The material used in this study is the 2$^{nd}$ generation single crystal Ni-based superalloy CMSX-4 and its composition is given in Table 1. A detailed investigation of its high temperature mechanical properties can be found in [13]. The alloy was supplied by ALSTOM in the form of <001> cylindrical rod castings. The batch received had undergone a proprietary commercial stepped solution heat treatment with a rapid gas fan quench in argon followed by a single stage ageing heat treatment. The

resulting characteristic γ/γ' microstructure and the dendritic structure are shown in the SEM backscatter electron (BSE) images of Figure 1.

| Alloy | Cr | Co | Al | Ti | W | Mo | Ta | Hf | Re | Ni |
|---|---|---|---|---|---|---|---|---|---|---|
| CMSX-4 | 7.53 | 9.71 | 12.31 | 1.24 | 2.07 | 0.37 | 2.13 | 0.32 | 0.96 | 63.37 |

Table 1: Nominal composition of the single crystal Ni-based superalloy CMSX-4 (at.%)

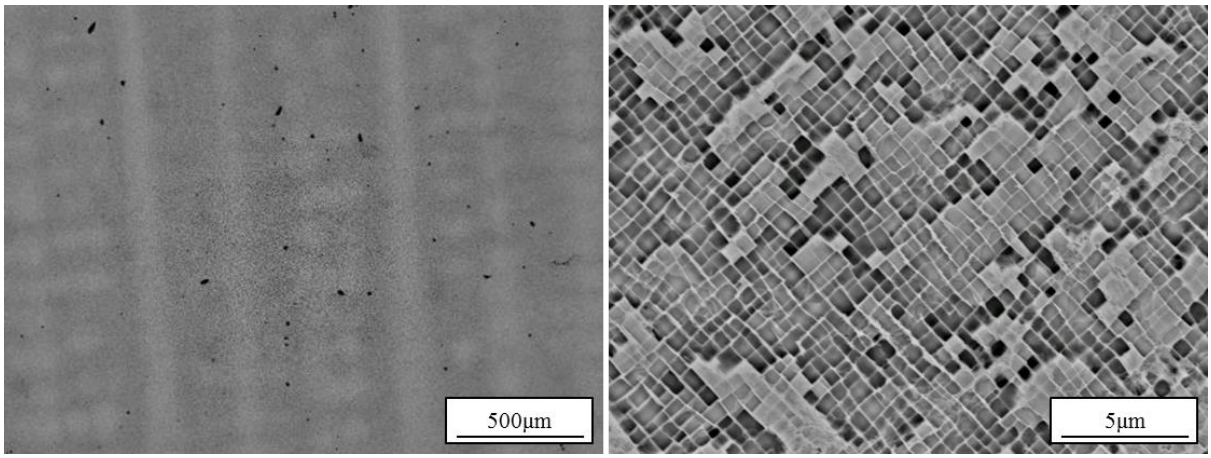


Figure 1: SEM BSE images of the fully heat treated CMSX-4 showing a) dendritic structure and porosity mainly concentrated within the interdendritic regions and b) cuboidal γ/γ' microstructure

## 2.2 Mechanical testing

Fatigue testing was conducted on a 50kN INSTRON 8501 servo-hydraulic machine retrofitted with a high temperature vacuum chamber which utilises four high intensity quartz lamps. All tests were conducted at 550°C and the temperature was controlled to ±1°C by an R-type thermocouple spot welded on the side surface of the samples. Single edge notched bend (SENB) specimens with a cross-section of 9mm x 9mm were tested in three point bending with a loading span of 40mm. A through thickness starting notch of 2.25mm was machined at the centre of each sample by electrostatic discharge machining (EDM). During testing, the tensile axis (TA) was parallel to the <001> direction while the EDM notch was along the <010> direction. A schematic of the sample set up, dimensions and orientation is shown in Figure 2a. Figure 2b shows a 3D representation of the dendritic structure of CMSX-4 (aligned with the sample) constructed by taking optical microscopy images of etched surfaces aligned with the (001), (010) and (100) planes.

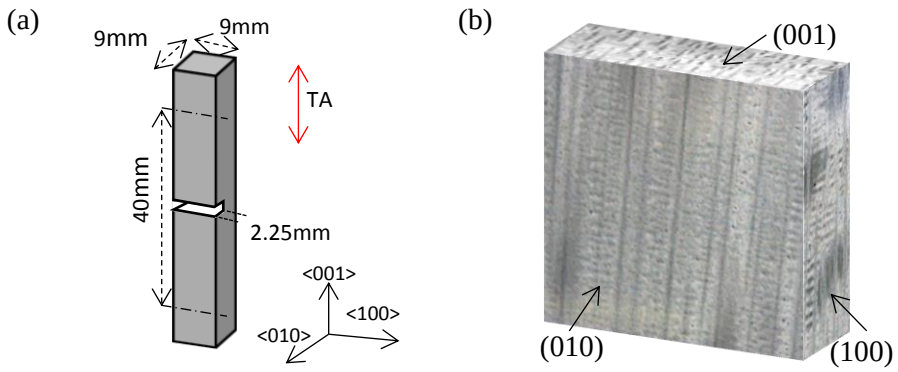


Figure 2: (a) Schematic diagram of the SENB samples used for fatigue testing with coordinate system showing crystallographic orientations and (b) 3D reconstruction of optical microscopy images showing the dendritic structure on 3 planes

Cyclic loading for all testing was applied under load control, using a load ratio of R=0.1 and a trapezoidal waveform of the type 1s – Xs – 1s – 1s, with the 1s segments corresponding to the load ramping periods and the dwell at minimum load, while hold time at maximum load (X) was varied between tests. The FCP rate was monitored continuously using the direct current potential drop (DCPD) method. A set of PD probes was spot welded across the notch, while a second set was attached away from the propagating crack to provide a far field reading for normalisation against temperature and current variations. An experimentally obtained calibration function was used to relate the crack length ($a$), sample width ($W$) ratio to the normalised PD. To ensure accurate values, the derived crack lengths were checked and re-calibrated post-test, against beach marks formed on the fracture surface. The FCP rates were derived from the curve of the variation in the electrical potential with time using the secant method. Prior to testing, the specimens were pre-cracked at the testing temperature (550°C) using a load shedding method with a 2.5Hz sinusoidal waveform, stress ratio of 0.1 and an initial stress intensity range factor $\Delta K = 20MPa\sqrt{m}$. The $\Delta K$ was stepped down in 10% increments after the crack had grown through four (plane stress) monotonic plastic zone sizes until a $\Delta K=15MPa\sqrt{m}$ was achieved.

The experimental work included three different types of tests as outlined below:

i. **Fatigue crack propagation tests (constant load, increasing ΔK)** were conducted to obtain the characteristic crack growth rate vs. stress intensity factor range graph for CMSX-4 in air and in a low oxygen partial pressure environment (referred here as “vacuum”), in order to

assess the effect of oxidation. A total of two tests were conducted (air and vacuum), using a "baseline" trapezoidal waveform of 1s – 1s – 1s – 1s starting at a ΔK = 15MPa√m and run to failure at a constant load, with increasing ΔK. For the vacuum test, the chamber was pumped down to $10^{-7}$bar and was then filled with Nitrogen to 1bar. By then re-evacuating the chamber again to $10^{-7}$bar and assuming perfect mixture of gases, the oxygen partial pressure during testing was estimated to be at the order of $10^{-15}$bar.

ii. **Frequency scan tests (constant ΔK = 20MPa√m, $K_{max}$ = 22MPa√m)** were employed to examine the effects of frequency/dwell on the FCP rate at a fixed ΔK (and $K_{max}$). The ΔK value was selected to be within the low-mid end of the Paris regime in order to achieve a FCP rate low enough for significant oxidation processes to take place at the crack tip and at the same time to allow accurate control of the ΔK during load shedding. During the test, eight different loading frequencies were used ranging from 0.005Hz to 5Hz. For frequencies up to 0.25Hz, the trapezoidal waveform (1-X-1-1) was used, whereas for higher frequencies a sinusoidal waveform was employed to allow a more accurate servo-hydraulic response. The frequency test sequence was arranged such that a high frequency testing period was followed by a low frequency one. This caused distinct changes in the fracture surface which were later used to calibrate the measured crack length to the monitored PD. At each frequency, the crack was allowed to grow approximately 0.4-0.5mm corresponding to 4-4.5 monotonic plane stress plastic zone sizes.

iii. **Alternating dwell or "Block tests"** were conducted to assess the effect of oxidation ahead of a crack tip. Such tests (termed "block tests") were previously employed to identify the extent of oxidation induced damage ahead of a crack tip in a polycrystalline Ni-based superalloy [14]. By switching between regimes of low and high frequency and examining the transitions in crack growth behaviour, the extent of the crack tip damage formed under particular conditions (i.e. the interaction between strain rate and oxidation) can be examined. These tests were run to failure with increasing ΔK by alternating between short and long dwell waveforms for crack increments equal to at least 4 plane stress plastic zone sizes. Figure 3

shows a schematic of the loading applied. Based on the frequency scan test results, representative dwell times were selected to induce different propagation mechanisms; 1s was selected as the baseline (short) dwell while 90s, 180s and 300s were used as the long dwells in different samples. Two of these tests were interrupted at crack lengths of $\alpha_1 = 6.1\text{mm}$ and $\alpha_2 = 6.4\text{mm}$ and held under sustained load (corresponding to K values of $K_1 = 34\text{MPa}\sqrt{\text{m}}$ and $K_2 = 28.5\text{MPa}\sqrt{\text{m}}$) for 12h. During the hold period any crack growth was monitored with the DCPD method. Subsequent baseline fatigue crack growth rates were then monitored to assess the effect of these hold times.

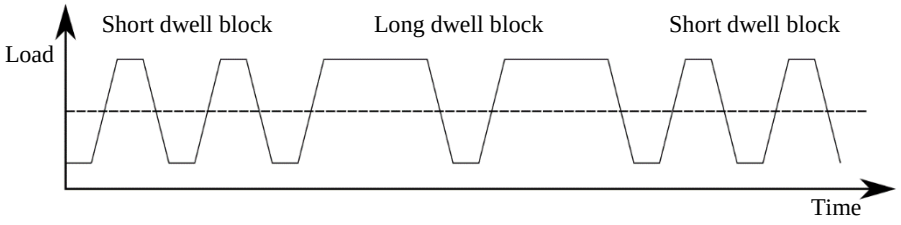


Figure 3: Loading waveform utilised for block tests.

## 2.3 Characterisation methods

The fracture surfaces were examined using a Wild M420 macroscope, an Alicona Infinite Focus microscope (IFM G4) and a JEOL JSM 6500 FEG-SEM at an acceleration voltage of 15kV. For the crack tip investigations, the interrupted test specimens were sectioned perpendicular to the crack front and a volume containing the crack was extracted as shown schematically in Figure 4a. The extracted sample was mounted in conductive bakelite and polished down to 0.02μm OPA for SEM and EDS investigation of the crack tip surface.

Microanalysis of the crack tip region was performed by extracting TEM thin foil samples by FIB milling in a Versa 3D dual beam system consisting of a focused gallium ion beam and a FEG SEM. The TEM samples were extracted parallel to the sample surface in order to allow examination of the crack tip and of the material ahead of it (Figure 4b). The TEM foils were then examined in a Talos F200X (STEM mode) equipped high resolution energy dispersive spectroscopy (EDS).

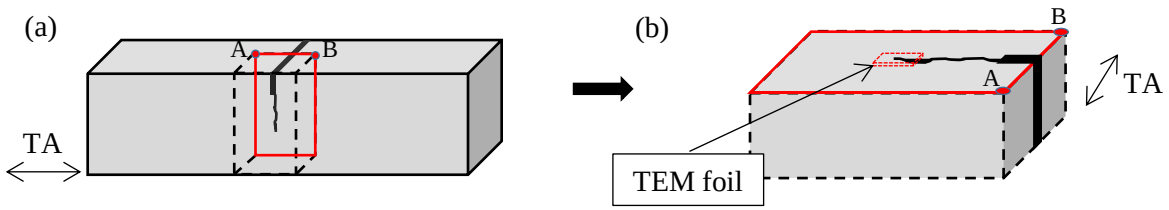


Figure 4: Schematic illustration of the interrupted test samples showing the TEM foil location and extraction: (a) interrupted test sample showing the volume extracted around the crack region for SEM investigation, (b) location and orientation of the TEM foil sample

# 3 Results

## 3.1 Fatigue crack growth in air and vacuum

Figure 5a compares the FCP rates of CMSX-4 at 550°C in air and vacuum, under the baseline conditions of 0.25 Hz (1-1-1-1 waveform). From the results, the FCP rates seem to be unaffected by the environment and both fracture surfaces appear macroscopically smooth and flat within the FCP region, indicating a predominantly stage II propagation. The (001) "**+**" dendritic structure is more evident on the fracture surface produced in vacuum which has experienced less oxidation. Both tests exhibit some degree of side faceting (crack growth along {111} planes) with the features being more pronounced in vacuum (Figure 6b and c). Figure 6 shows SEM images of the fracture surfaces of the two tests at a $\Delta K$ level of 30MPa$\sqrt{m}$. Both surfaces exhibit a blocky morphology with the $\gamma$ matrix in the air test appearing heavily oxidised. Evidence of $\gamma$' shearing can only be seen on the fracture surface of the vacuum test in Figure 6b.

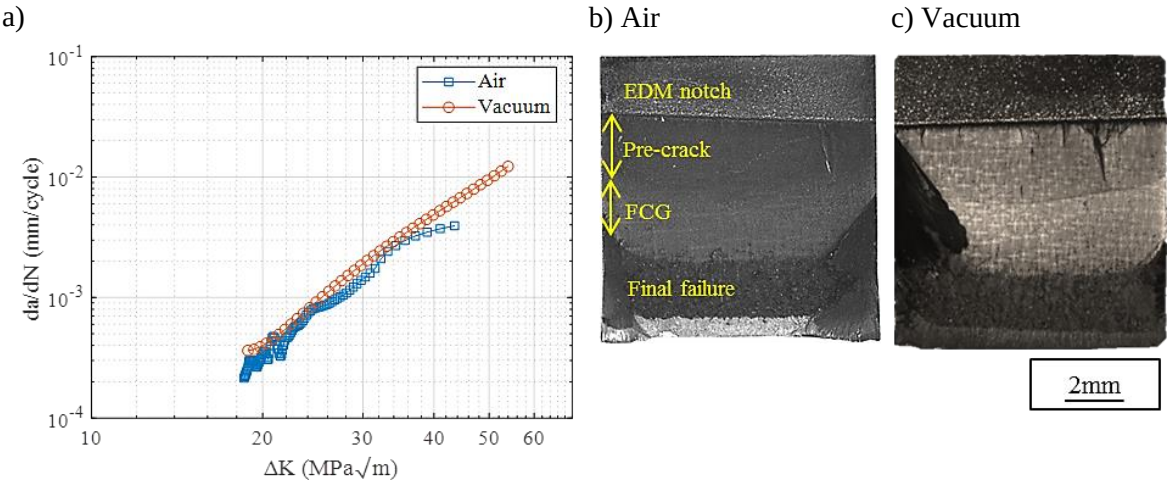


Figure 5: a) Fatigue crack propagation rates in air and vacuum for CMSX-4 at 550°C, b) and c) fracture surface overviews of the air and vacuum tests.

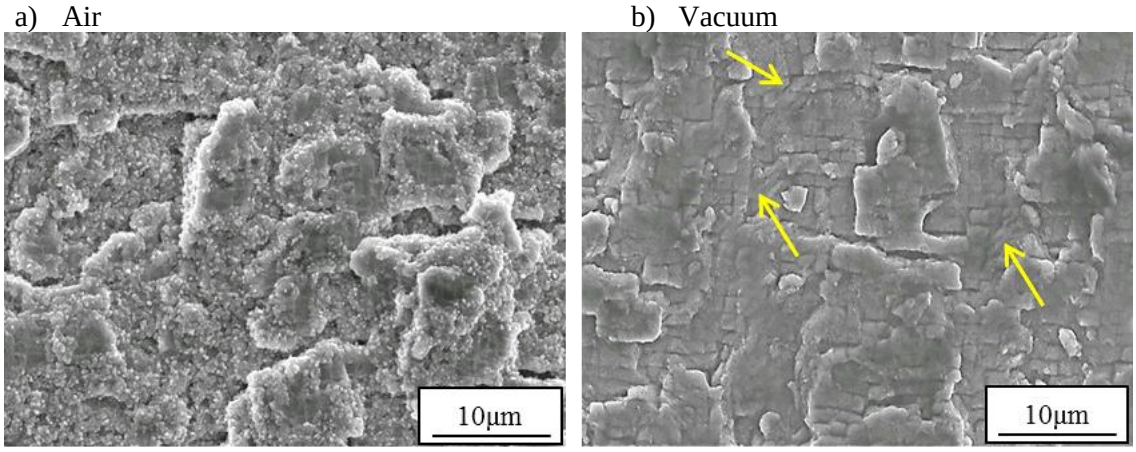


Figure 6: SEM images of the fracture surface (ΔK~30MPa√m) of CMSX-4 samples tested in a) air and b) vacuum at 550°C. The yellow arrows on b) show locations with evidence of γ' shearing.

## 3.2 Effects of frequency on fatigue crack propagation (constant ΔK)

The effects of frequency on the FCP rate are shown in the crack length against time plot (Figure 7) obtained from the frequency scan test (constant ΔK=20MPa√m). The discontinuities of the plot represent the transition growth data which were discarded to ensure that only the stable growth of each frequency regime was further analysed.

The fatigue crack growth rates derived from the different regions are shown in Figure 8 on the basis of (a) cycles ($\frac{da}{dN}$) and (b) of time ($\frac{da}{dt}$) against frequency. In both plots, the FCP data can be fitted

with two straight lines described by a power law, where the exponent is the slope of the line on the log-log plot. In Figure 8a the FCP rate increases with decreasing frequency with a slope of -1.04 for frequencies lower than 0.043Hz (corresponding to 1-20-1-1 waveform). In this region FCP rates become inversely proportional to the loading frequency (time dependent) and the dwell time controls crack propagation rates. This is also evident in Figure 8b where the time required to grow the crack by a specific length appears to become constant at the lowest frequencies. On the other hand, at frequencies higher than 0.043Hz the slope of the curve in Figure 8a approaches 0 indicating a cycle dependent FCP.

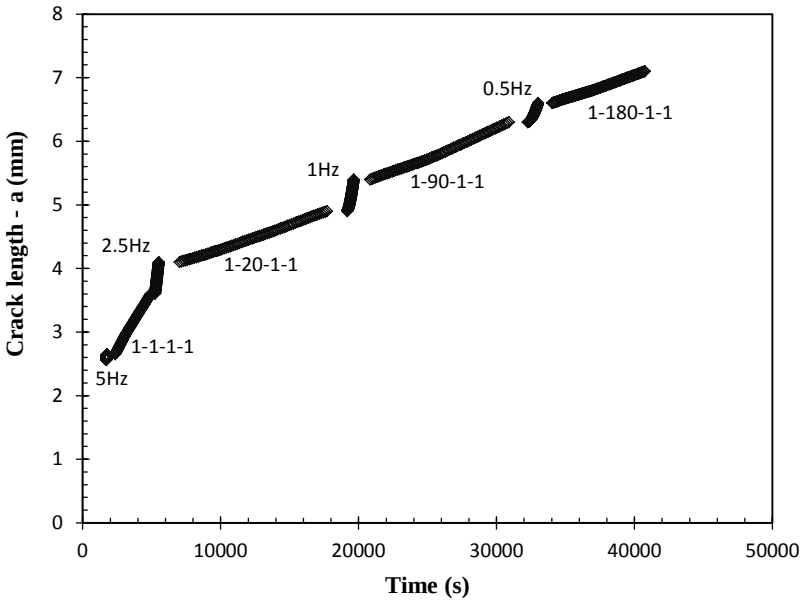


Figure 7: Fatigue crack growth behaviour of CMSX-4 at a constant ΔK of 20MPa√m at 550°C under different loading frequencies/waveforms. At the bottom left of the plot the fracture surface of the CMSX-4 sample used is shown.

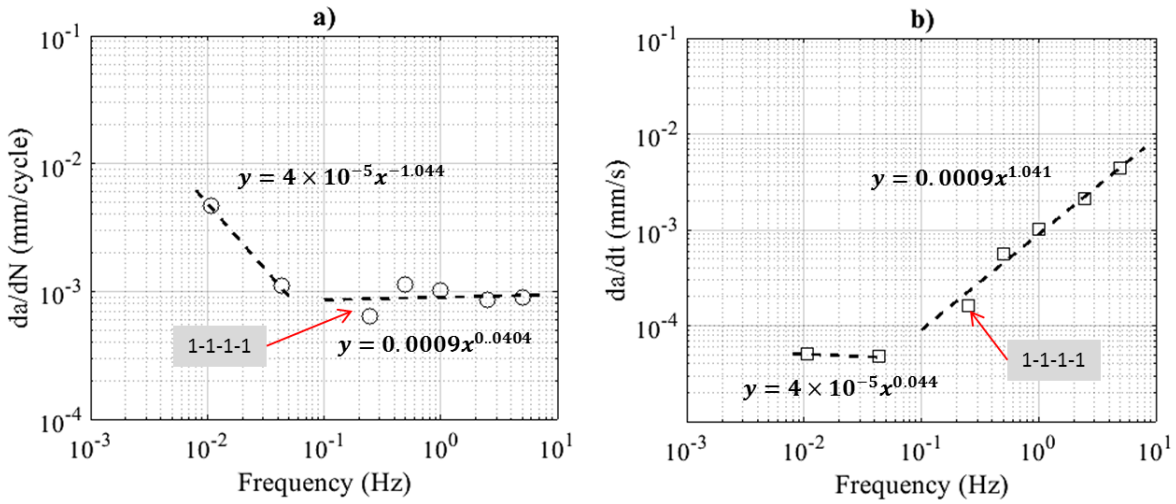


Figure 8: Effect of frequency on the crack growth rate of CMSX-4 at 550°C (at a constant ΔK~20MPa√m) on the basis of: a) cycles and b) time.

A topological surface map of the fracture surface created with the built-in 3D Image-Field feature of the Alicona microscope is included is shown in Figure 9a to illustrate the distinct markings (beach marks) formed due to changes in the propagation mechanism with alternating frequency. Figure 9b-h shows high magnification images of the different areas on the sample, associated with propagation at a specific frequency, arranged in order from the highest to the lowest frequency. The location of each region on the fracture surface of the sample is indicated on Figure 9a. At the higher frequency regions, the fracture surface appears smooth and flat, but progressively becomes more blocky and ratcheted as the frequency decreases. To quantify this, an Alicona 3D microscope was used to analyse the different regions in terms of their roughness. The results are presented in Figure 10 and show that both the average surface roughness (*Sa*) and the root mean square roughness (*Sq*) parameters decrease with increasing frequency. At this stage, it is important to note that fracture surfaces corresponding to frequencies tested earlier in the experiment had been exposed (post cracking) to high temperatures for longer and that some of their features might have been masked by oxidation (for the testing sequence refer to Figure 7 and Figure 9a).

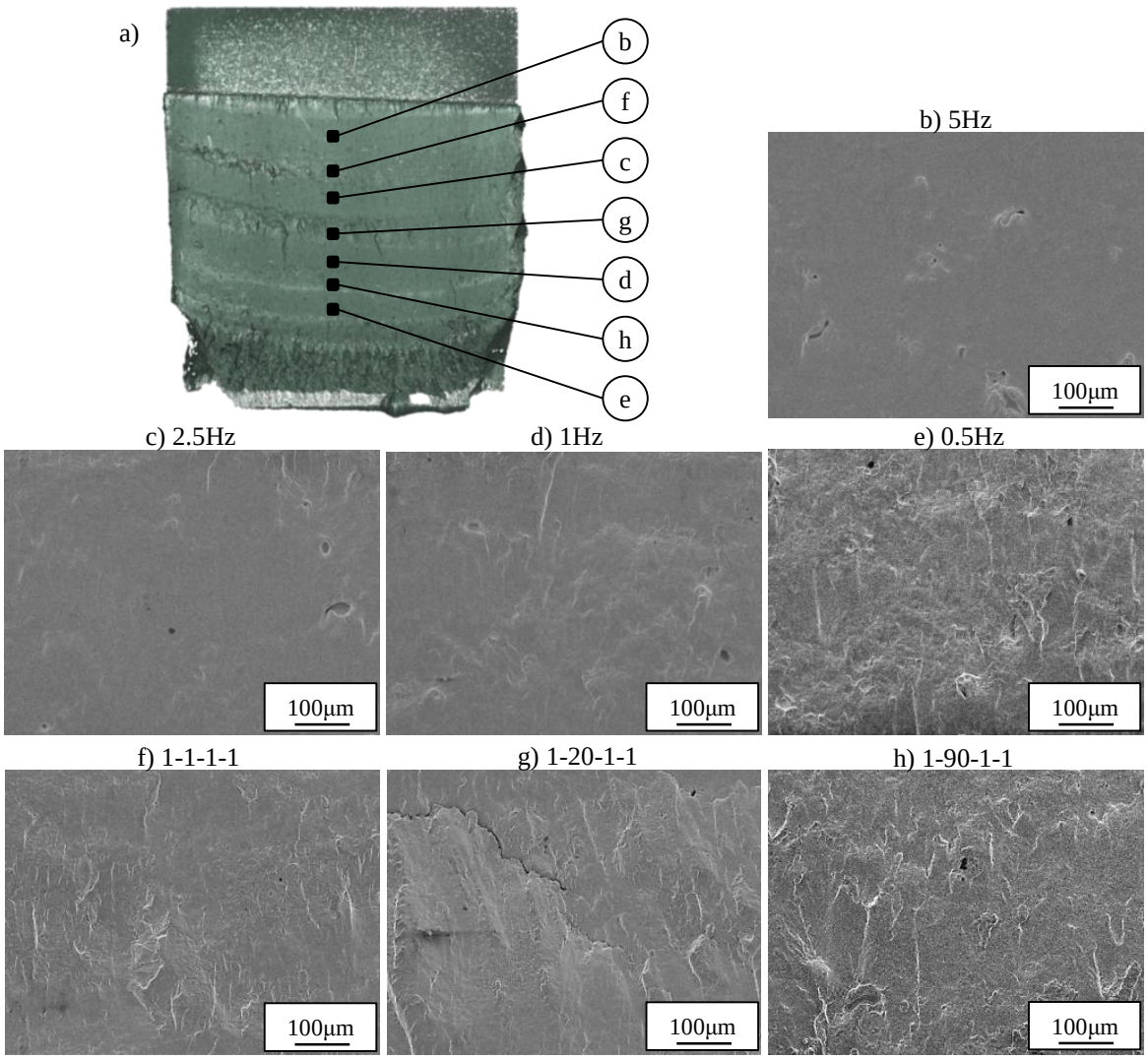


Figure 9: SEM fractography the CMSX-4 sample tested under constant ΔK at 550°C with alternating frequencies: a) Alicona image field overview of the fracture surface, b) - h) higher magnification images of regions formed under different frequencies in a descending order.

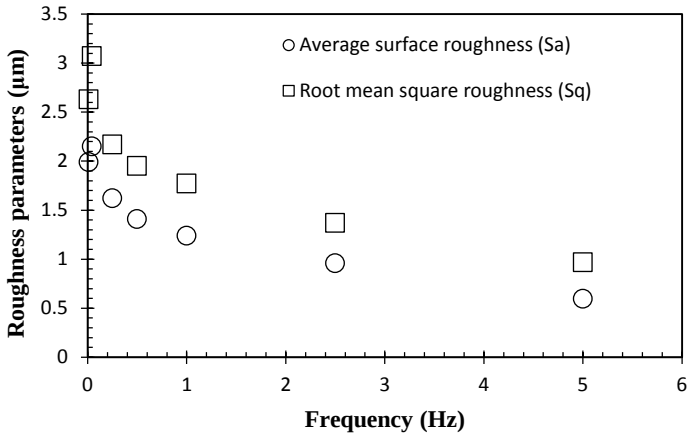


Figure 10: Roughness ($S_a$ and $S_q$) values obtained from the various frequency regions from the fracture surface of the CMSX-4 sample tested under constant $\Delta K=20MPa\sqrt{m}$ on the frequency scan test sample

## 3.3 Fatigue crack growth with alternating frequency (block loading)

The results from the frequency scan test indicated that time or mixed mode dependent fatigue crack growth would take place if a trapezoidal loading waveform with dwells longer than 20s is imposed at 550°C. Therefore, the long dwell times of 90s, 180s and 300s were selected for use in the block tests. The results from a total of five tests are shown in Figure 11. Among them, two 300s long dwell block tests were conducted with the transition from short to long dwell block taking place at intermediate and at high ΔK levels (shown as blue rhomboid and yellow circular data on Figure 11a). A third test was conducted with a long dwell block of 180s and the transition took place an intermediate ΔK (orange rectangular data in Figure 11b). In a similar manner, a fourth test having a long dwell block of 90s, with the transitions taking place at an intermediate ΔK, is shown in Figure 11c. Finally, a single specimen was used to examine a block of 300s dwells at low ΔKs and a block of 180s at high ΔK levels. The crack growth results from this test were therefore split into two and are shown in Figure 11a and Figure 11b for the 300s block (green rectangular data) and the 180s block (grey triangular data) respectively. The long dwell blocks are labelled and the 1-1-1-1 trendline from the test of Figure 5 was added for comparison to all figures. Table 2 shows the details of the tests conducted and the figure number upon which the results are displayed.

| Sample ID | ΔK of long dwell block | | | No. of transitions between blocks | Figure displayed |
|---|---|---|---|---|---|
| | low | mid | high | | |
| 1 | - | 300s | - | 2 | Figure 11a |
| 2 | - | - | 300s | 1 | Figure 11a |
| 3 | - | 180s | - | 1 | Figure 11b |
| 4 | - | 90s | - | 2 | Figure 11c |
| 5 | 300s | - | 180s | 2 | Figure 11a and b |

Table 2: Test matrix summarising the block tests

As can be seen from Figure 11, the crack growth results obtained during the long dwell blocks are generally associated with a significant amount of scatter and in almost all cases, the FCP rates decrease during the long dwell block (low frequency, time-dependent) part of the test. This is in contrast with the trend observed in the frequency scan test (at a constant ΔK of 20 MPa √m), where longer dwells corresponded to higher rates of da/dN. An exception to this is seen in the FCP rates (red square data) shown in Figure 11b, where an observable step increase occurs at higher ΔK levels (>27MPa√m), during the 1-180-1-1 block of the test. It is important to note that the entire growth rate data obtained from this sample (*Sample 5*) were noticeably higher than the baseline. This is also evident from the black rectangular data of Figure 11a, which were obtained from the same sample during propagation at low ΔKs. This is possibly attributed to a different (overall) propagation mechanism. All other samples have shown macroscopic stage II propagation with small amounts of side faceting, while significant stage I type growth was observed in *Sample 5*, particularly during the formation of extensive side facets. To illustrate this, the fracture surface of *Sample 5* is compared with that of *Sample 2* (purple circular data in Figure 11a) in Figure 12.

Figure 11b also includes the results obtained using *Sample 3*, where the transition from the short dwell block to the long dwell block (180s), took place at an intermediate ΔK range. The FCP rate, which initially seems to decrease, when the block changes from short (1s dwells) to long (180s dwells) at ΔK=24MPa√m, can be presumed to increase when the ΔK approaches 30MPa√m.

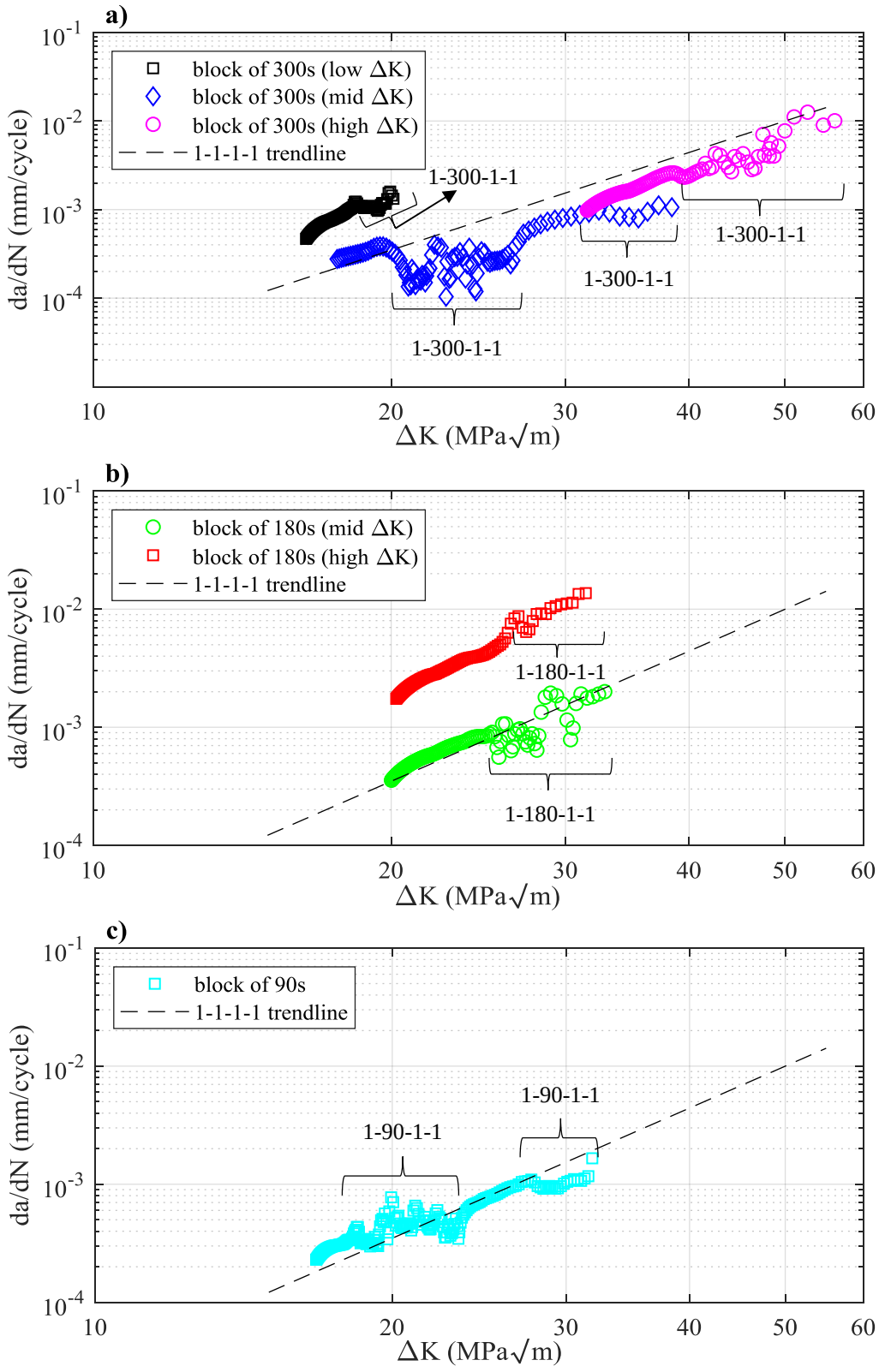


Figure 11: Fatigue crack growth rates from alternating dwell tests on CMSX-4 at 550°C: a) tests at low, mid and high ΔKs with 1s and 300s dwells, b) tests at mid and high ΔKs with 1s and 180s dwells and c) tests at low, mid and high ΔKs alternating 1s and 90s.

a)  b) 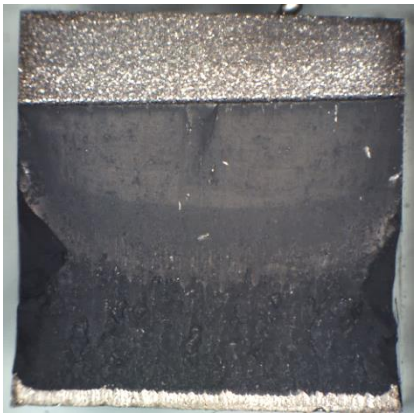

Figure 12: Fracture surface overviews of: a) sample 5 and b) sample 2

## 3.4 Crack tip characterisation

SEM BSE images of the two fatigue cracks that formed under a 12h sustained load at 550°C are shown in Figure 13a and Figure 13b. *Crack tip-1* was held at $K_{1_{opening}} = 34MPa\sqrt{m}$ and propagated for 15µm while *Crack tip-2* was held at $K_{2_{opening}} = 28.5MPa\sqrt{m}$ and propagated for 7µm during the 12h hold. Both crack tips have a complex morphology with multiple branches emanating from the main body. Evidence of oxidised γ'along the branches of both tips were observed, but with no indications of an oxide-induced damage zone ahead of them. The complexity of the propagation mechanism can be realised in Figure 13c and Figure 13d from the high magnification STEM high angle annular dark field (HAADF) images of the foil specimens extracted from the crack tips of both samples. The extracted foils are shown below Figure 13a and Figure 13b and their locations are indicated by the dotted rectangles.

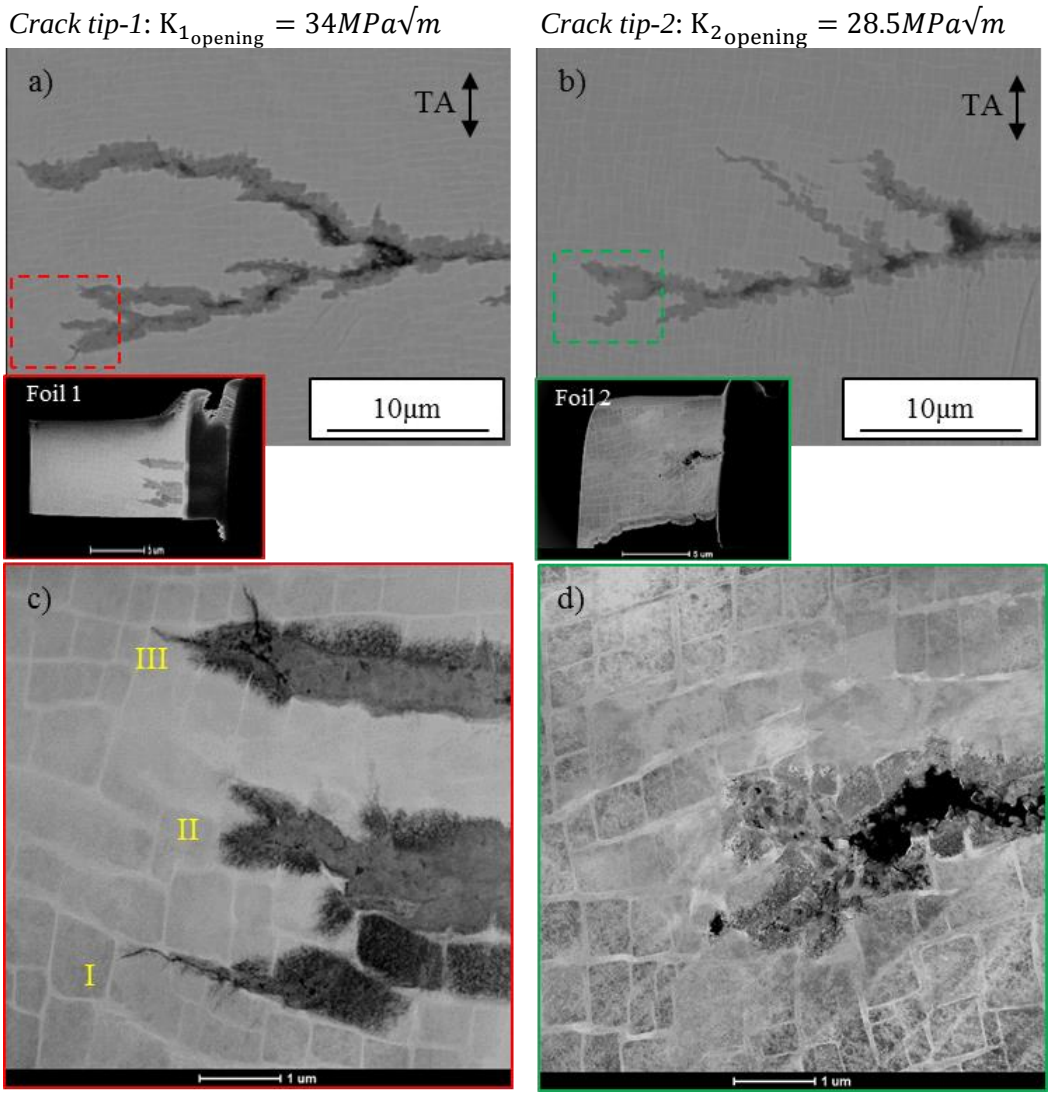


Figure 13: a) & b) SEM BSE images of the crack tips formed under sustained load for 12h at 550°C. The loading axis is shown at the top right of each image and the location of the TEM foils is indicated by the dotted rectangles, c) & d) HAADF STEM images of the crack tips with the individual branches marked as I, II and III.

Figure 14 shows high magnification bright field (BF) and HAADF images of the three branches of *Crack tip-1*, shown in Figure 13c, accompanied by EDS element maps. From these high magnification images, it is apparent that the crack propagates both near the γ/γ'interface and by shearing the γ' particles. The oxidised crack tip of branch I can be seen to predominately propagate near the γ/γ' interface, before it deflects by approximately 45° degrees from the loading axis (Figure 14a) . Branch II, which itself branches out in two sub-tips shows a similar behaviour (Figure 14b). The upper sub-tip appears to have propagated along the γ channel while the lower sub-tip penetrated an oxidised γ' particle. Branch III appears to be generally moving along the γ/γ' interface but its tip is seen arrested

within a γ’ particle (Figure 14c). Co and Ni-rich oxides forming on the surfaces of all three branches are observed to bridge the crack near the tip. Just below these external oxides, a Cr-rich oxide formed a thin band. Internally, within a Ni-depleted zone, Ti and Al-rich oxides formed finger-like protrusions which penetrate the material ahead and around the crack tip. The penetration depth of the oxide for crack tip 1 ranges between 50-150nm. The STEM EDS maps of *Crack tip-2* are illustrated in Figure 15. This is a less complex crack tip with only two branches propagating at approximately 45° to each other. The oxide layer sequence and the penetration depths at the tips of the two branches are similar to *Crack tip-1*. The edges of the tips are less defined compared to *Crack tip-1*and the crack appears more open.

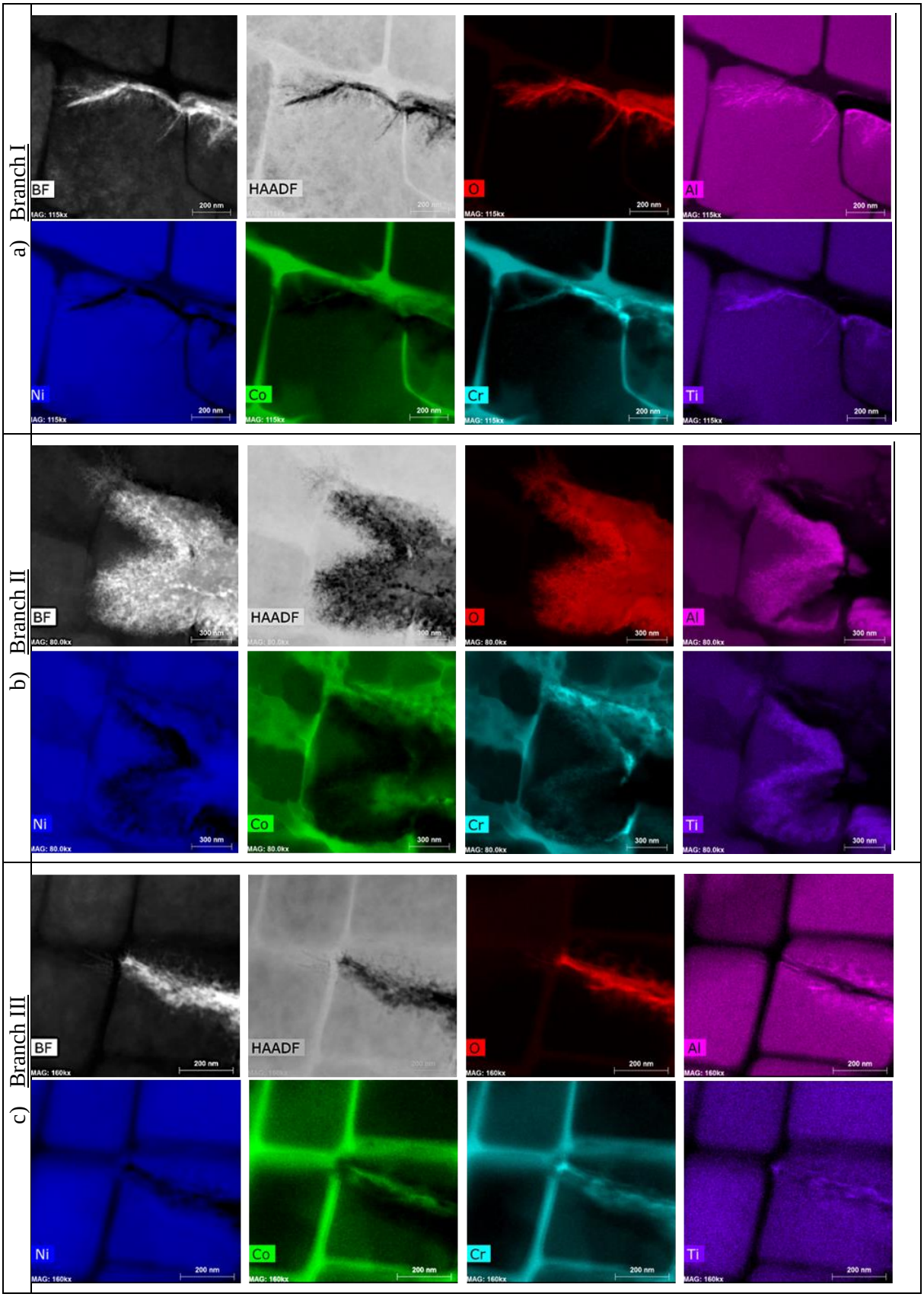


Figure 14: STEM-EDS maps of *Crack tip-1* branches formed at constant load $(K_{1_{opening}} = 34MPa\sqrt{m})$ for 12h at 550°C

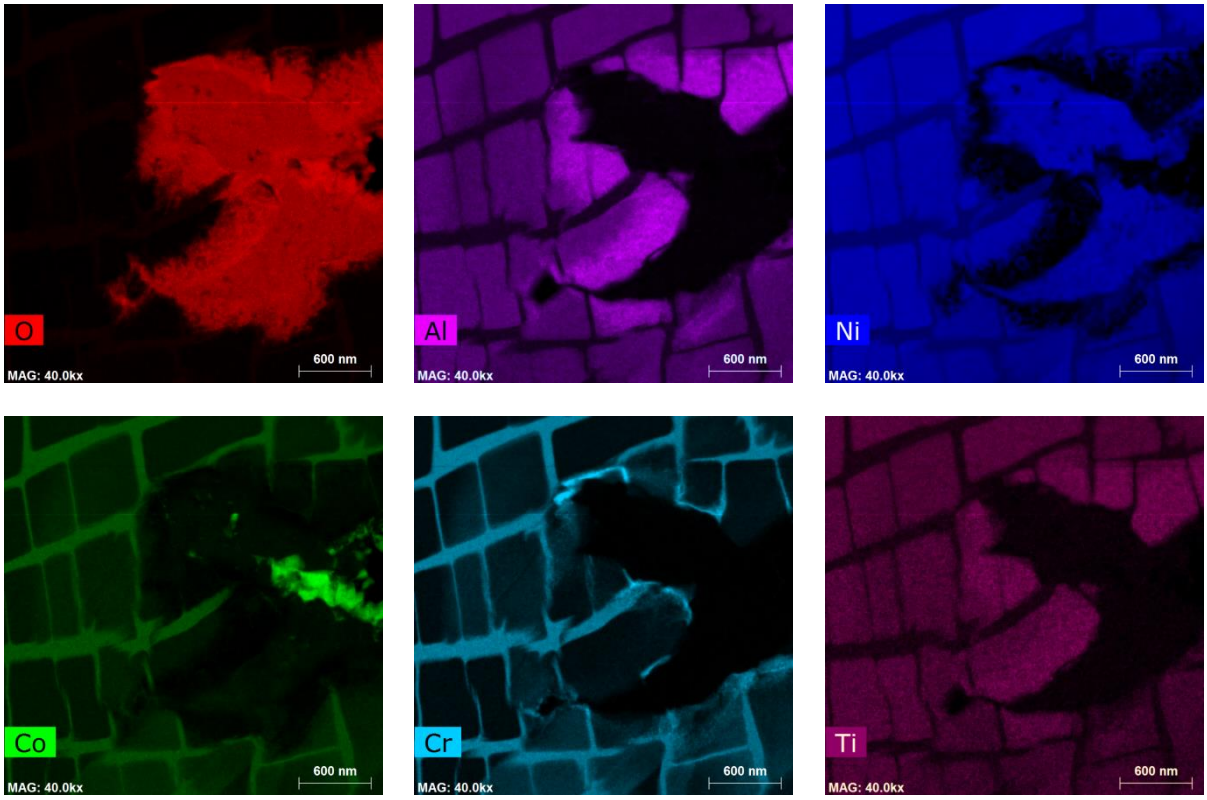


Figure 15: STEM-EDS maps of *Crack tip-2* formed at constant load ($K_{1_{opening}} = 28.5MPa\sqrt{m}$) for 12h at 550°C

# 4 Discussion

## 4.1 Effects of oxidation on the fatigue crack growth behaviour

At low to intermediate ΔK levels crack growth at 550°C, in both air and vacuum, takes place macroscopically along the {100} plane with an overall Stage II mode. Stage II growth at elevated temperatures is generally attributed to thermally activated deformation processes such as dislocation climb or cross slip [12,15]. In addition, planar slip bands, which contribute to Stage I crack growth, can be suppressed by oxidation which then leads to homogenisation of the slip process, making Stage II behaviour more favourable [16]. However, such processes have been generally observed during fatigue at much higher temperatures in similar systems, e.g. [15,17,18]. Even though the fracture surface of the 550°C test was obscured by oxidation and thus fractography could not yield conclusive results, similar processes could be presumed to be active here as well. This is because oxidation and other thermally activated processes, not only depend on temperature but also depend on time, and the

0.25Hz frequency (1s-1s-1s-1s waveform) used in this study is much lower than those used in the aforementioned research. As noted by Leverant and Gell [15], another condition for Stage I to occur is that the crack must form along the slip band faster than the time needed for dislocation recovery out of the bands themselves. This suggests that, even at lower temperatures, given that the frequency is low enough, there could be enough time for the dislocations to cross slip out of the planar bands before the crack manages to grow along them; therefore promoting Stage II propagation.

Despite the macroscopic Stage II appearance, evidence of γ' cutting has been found on the fracture surfaces of the test in vacuum, suggesting a more complex propagation mechanism (Figure 6b). Fundamentally, the critical resolved shear stress in FCC single crystals is much lower along the {111} planes and thus deformation is easier compared to the {100} planes [13]. In addition, it is well established that the coherent γ' precipitates can be more easily sheared at low temperatures (peak strength of γ' is seen at approximately 700ºC) [19]. Therefore, it is possible for the fracture surfaces to contain evidence of sheared precipitates by {111} type slip bands at these temperatures. Notably, γ' shearing was only observed at intermediate and high ΔKs in the 550°C test in vacuum, indicating that 550°C is sufficiently high to activate significant homogenisation of slip, if the crack growth rate (and crack tip opening) is low enough.

At high ΔK levels, near fracture, the fatigue crack growth became purely cycle dependent (propagation along alternating {111} planes) for both temperatures and environments. This type of propagation can be explained by the alternating shear model proposed by Neumann [20]. The model suggests that when a crack is propagating along the primary slip plane, the slip system ahead of the crack tip work hardens due to dislocation accumulation, shifting the crack tip to a plane where a softer slip system operates. Thus the crack frequently changes the growth direction from one slip system to another to essentially follow the path of least resistance.

Extensive slip-band cracking with faceted <111> crack growth can also take place locally in the vicinity of porosity, where complex local stress states may be expected to occur. Similar observations were seen on the fatigued surfaces of CMSX-4 samples at 650ºC under a 1-1-1-1 waveform [5]. The authors noted that porosity had promoted transition to alternating slip band cracking by providing

local stress concentrations. Planar slip can be therefore promoted around defects of a certain size at ΔK levels lower than the ones required to produce extended slip band cracking across the whole sample. This behaviour is of particular interest when the interdendritic regions are considered where porosity is mainly concentrated.

The FCP rates at 550°C in air and vacuum were very similar. This suggests that oxidation has negligible effects on the long crack fatigue performance at these temperatures and frequencies. Testing conducted on CMSX-4 at a similar temperature (650ºC ) by M. Joyce et al. [5] showed faster FCP rates in vacuum compared to air. The faster crack growth rates seen in vacuum were attributed to the homogenising effect of oxidation on slip which not only suppressed faster Stage I crack growth but possibly increased oxidation-induced closure. Henderson and Martin [17] reported similar behaviour in another SX Ni-based superalloy (SRR-99), also at 650°C. Fractographic analysis conducted in both of these studies showed that the crack path followed the γ/γ' interface at low to mid-ΔK levels. Contrary to this study, the fracture surfaces of the samples tested by M. Joyce et al. [5] showed less Stage I growth, particularly when comparing side facet formation (refer to Figure 5). Previous work on U720 single crystal, has shown that Stage I type crack growth is fundamentally more rapid than Stage II under the same applied stress levels (given that closure effects are accounted for) [21]. Hence, the interaction between the faster Stage I crack growth and oxidation induced retardation mechanisms would be expected to be competing in this study.

## 4.2 Mixed time and cycle fatigue crack growth dependence

The results shown in Figure 8 indicate that a dwell of 20s or longer ($f$ < 0.043Hz) is sufficient to activate time-dependent damage processes. Comparing with the results of Figure 5, where the FCP rates in vacuum and air obtained with 1-1-1-1 waveform ($f$ = 0.25Hz) are very similar, it can be deduced that (at ΔK=20MPa√m) a transition frequency between 0.25-0.04Hz exists where environmental damage will contribute to the overall growth rate.

To investigate the nature of the propagation mechanism in air further, a section was taken perpendicular to the fracture surface of the 550°C test and secondary cracks were examined under the

SEM in the plain polished and etched conditions as shown in Figure 16. Observations confirmed that the crack predominantly propagates through the γ/γ' interface, although some precipitate cutting is occasionally observed (Figure 16a). This indicates that a mechanism other than pure crystallographic or faceted crack growth (characteristic of cycle dependent damage) is taking place during 1-1-1-1 loading (0.25Hz). Depending on the ΔK level (and R-ratio [22]), the transition between cycle and time dependent fatigue is known to shift [23]. In agreement with previous studies, this transition spans over a range of frequencies where synergistic mechanical-environmental damage takes place [23,24]. It is therefore possible that at 550°C, frequencies lower than 0.25Hz promote a mixed time/cycle dependent damage. Pure time dependent crack growth would then require even longer dwells.

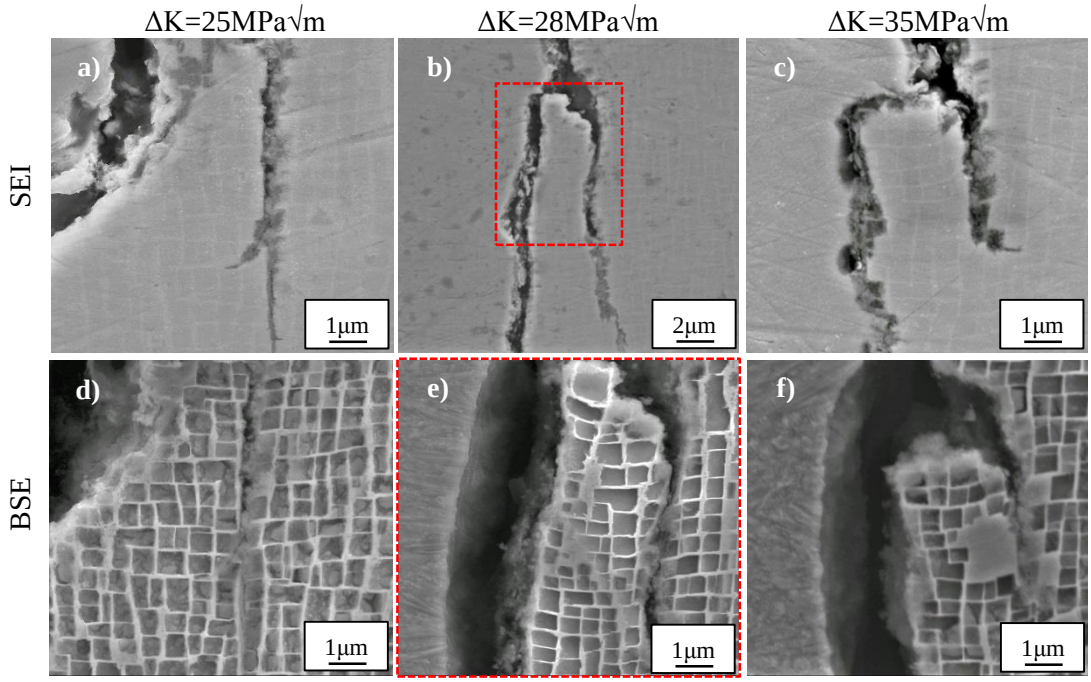


Figure 16: Secondary cracks in SEI and BSE mode penetrating the fracture surface of CMSX-4 fatigued at 550°C

Assuming a mixed time/cycle dependence regime, at lower ΔK levels, where FCP rates are slower, thermally activated processes and oxidation induced closure can significantly affect the fracture mode and effective driving force. Meanwhile, at higher ΔKs, the time allowed for $O_2$ diffusion at the near tip surfaces before the crack propagates further is potentially inadequate for the oxide to thicken enough and cause bridging of the surfaces. In addition, the mechanism of FCP was found to change

significantly under the effect of oxidation when the loading frequency is changed. The exponential increase in the measured roughness parameters (Figure 10) indicates that prolonged tensile stresses (i.e. lower frequencies) in the presence of $O_2$ create a more complex crack front. This could be linked to an increased amount of bifurcations and branching resulting from stress/strain assisted oxygen diffusion ahead of the crack tip and localised damage. Recent work that examined arrested cracks in a polycrystalline Ni-based superalloy in air and vacuum employed micro X-ray CT to quantitatively analyse the amount of branching/secondary cracks near the crack tip region [25]. Their results revealed that oxidising environments promote more micro cracks and crack bifurcations at the vicinity of the crack tip.

The complexity of the mechanisms operating during fatigue at 550°C was also illustrated from the results obtained by the block tests of Figure 11. According to the frequency scan test results, alternating between a cycle dependent regime (1-1-1-1) and a time or mixed dependent regime (1-90,180,300-1-1) the FCP rates should increase. In addition, according to the results of [9,14] the embrittling effects of oxidation should be evident and a damage zone ahead of the crack tip would be expected to promote higher FCP rates at least within its extent. Instead, FCP rates are found to decrease for the majority of the tests at all $\Delta K$ levels. Oxide induced crack closure is expected to be more dominant at lower $\Delta K$ levels because of the smaller crack tip opening displacements (CTOD) during a fatigue cycle. Given sufficient time, the thickness of the fracture surface oxide layer can become comparable in size to the CTOD resulting in crack face contact and reduction in the observed $\Delta K$. This is evident from the SEM-EDS maps of Figure 17 obtained at the wake of the crack from an interrupted block test (1s and 300s blocks). The fracture surfaces were formed at a $\Delta K=21MPa\sqrt{m}$ and lie within the 300s dwell block of the test. It is clear that the oxides formed are in contact at a number of points but at the same time it should be taken into account that the crack surfaces have been exposed to high temperature post cracking for the duration of the test (approx. 15h). Assuming pure mode I loading the CTOD can be expressed as [26]:

$$\delta = \frac{{K_I}^2}{\sigma_y E m}$$

where $m$ is a constant and equals to 1 for plane stress and 2 for plane strain conditions. $K_I$ , for the specific crack length equals to 23.3MPa√m. The yield stress ($\sigma_y$) and Young's modulus ($E$) along the <001> direction at 550°C are taken from in house testing as 900MPa and 120GPa respectively and the resulting CTOD was found to be 2.5µm. A previous study [27] has shown that the rate at which oxidation builds up on the surface of CMSX-4 at 550°C can be described by:

$$X^{6.2} = 3.44 \times 10^{-5} \times t$$

where $X$ is the thickness (µm) of the oxide scale building on a surface (under isothermal conditions) and $t$ is the exposure time in hours. Taking $t=0.08h$ (for 300s dwell) the oxide scale thickness ($X$) on each fracture surface is calculated to be 0.126µm, giving a total thickness (accounting for both surfaces) of ~0.25µm. Assuming no significant oxide spallation during cyclic loading, this indicates that, for a 300s dwell, the crack tip would be filled with oxides within 10 cycles, which could explain the reduction in FCP rates observed during the long dwell blocks.

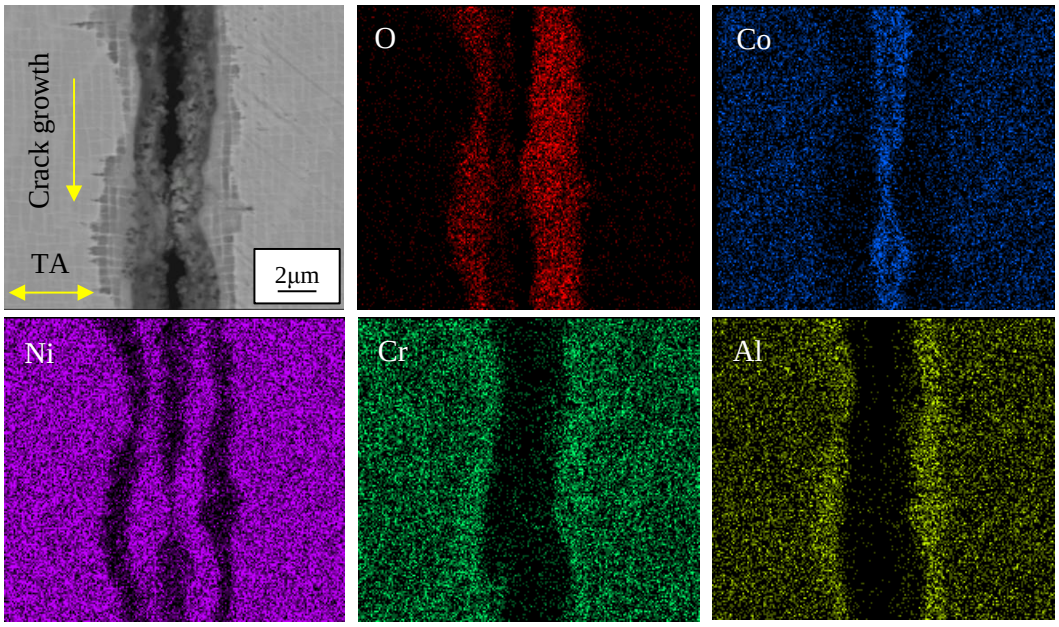


Figure 17: EDS mapping of the oxides formed on the crack surfaces at ΔK=21MPa

### 4.3 Damage ahead of a crack tip during dwell fatigue

The effects of long dwells and oxidation on the damage at a fatigue crack tip have been investigated by holding pre-cracked samples at a sustained load for 12h. According to the STEM-EDS results of Figure 14 and Figure 15, the oxide layering sequence at the crack tip, beginning from the innermost oxide, was Al→Ti→Cr→Ni→Co-rich oxides. Interestingly, previous work [27] on the isothermal oxidation of CMSX-4 at 550°C, did not show evidence of Cr or Co oxides forming even after 640h of exposure, which is significantly longer than the crack tip exposure during 1 cycle. However, evidence of Co-rich oxide forming externally on CMSX-4 was observed in samples that have been exposed at 550°C while held under tensile loads (Figure 17). The thermodynamic driving force for the oxidation of Co is similar in magnitude to that of Ni at 550°C and the fact that Co is only observed on strained surfaces implies that the rate of formation (kinetics) is directly affected by the stress state of the substrate.

Contrary to polycrystalline Ni-based superalloys, where oxidation can readily attack grain boundaries and contribute to higher FCG rates [28,29], the effects of environmental damage in equivalent single crystal alloys can be twofold. Depending on temperature, load ratio and frequency, two opposing mechanisms can influence the crack growth: (i) decrease of the FCG rate resulting from a reduction in the effective $\Delta K$ (or of the crack opening threshold) arising from oxide induced closure taking place near the tip and at the wake of the crack [5,30,31]; (ii) increase in the FCG rate by time dependent embrittlement ahead of the crack tip due to increased $O_2$ diffusion promoted by prolonged stresses at high temperature [8,9,32].

Based on the findings of this work and the associated literature, two possible damage mechanisms are proposed to be acting on the crack tip during fatigue and oxidation interactions. The first mechanism involves propagation of the crack by failure of an embrittled volume ahead of the crack tip. The effects of such a mechanism would be realised at a microscopic level and its extent would be analogous to the size of a microstructural feature that is susceptible to oxidation. The second mechanism involves damage at the nanoscale by decohesion at an interface. Such a mechanism is generally encountered in intergranular failure in polycrystalline alloys and it is termed as dynamic

embrittlement. An equivalent mechanism could also be active during high temperature fatigue in single crystal superalloys, with the damage taking place at the γ/γ' interface.

The high magnification SEM and STEM images of Figure 13 and the STEM-EDS maps shown in Figure 14 - Figure 15 did not indicate extensive damage and oxide penetration was confined to within only a few tens of nm ahead of the crack. It is recognised though that propagation through a potentially damaged volume ahead of the crack tip might have taken place during unloading when retrieving the sample from the testing machine, even though there was no noticeable increase in the PD reading.

Naturally the absence of grain boundaries in single crystal superalloys makes them more resistant to time dependent damage mechanisms (e.g. creep, dynamic embrittlement). As anticipated at these temperatures, after careful examination of the TEM samples (Figure 13 - Figure 16), no indication of creep effects on the microstructure, such as rafting of the γ' and/or expansion of the γ channels [33], were found. Nevertheless, the difference in the lattice parameters of the γ and γ' phases represent a source of additional strain in the microstructure. The magnitude of this strain can be substantially increased in the case of exposure to high temperatures because of the difference in thermal expansion coefficients between the two phases. During the sustained load period in dwell fatigue conditions, the applied tensile load will further exaggerate the γ' tensile stresses and reduce the γ channel compressive stress parallel to the loading axis. Because of the Poisson effect, the opposite will take place in the direction perpendicular to the loading axis, i.e. the γ' interface tensile stresses are reduced and the γ channel compressive stresses will increase. If the loads are high enough, plastic deformation would take place first in the horizontal channels since the compressive stress in vertical channels will oppose deformation. As a result, an increased number of dislocations would accumulate in the horizontal γ/γ' interface, perpendicular to the tensile axis (parallel to the crack growth direction) [34,35]. An illustration of this process is shown in the schematic of Figure 18.

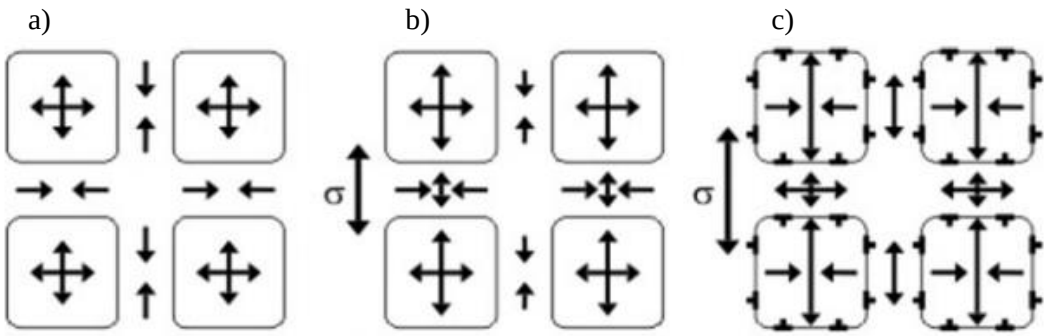


Figure 18: Schematic showing the stresses acting on the γ/γ'microstructure due to a) initial misfit, b) after application of an external load and c) after larger external stresses and small plastic deformation (after [35])

Single crystal Ni-based superalloys have been designed to achieve large negative misfit (-0.2 to -0.8%) at service temperatures (1000°C) [36]. Large misfits form denser interfacial dislocations networks in order to relieve the misfit stress and act as effective barriers to further gliding dislocations from entering and shearing the γ' [37]. However, the larger amounts of line defects (dislocations) concentrated around the γ/γ' interface could act as low resistance paths for oxygen ingress. As shown in the study of Karabela et al. [38] the extent of oxygen induced damage at a fatigue crack tip depends on oxygen concentration/oxygen partial pressure and the stress state. Higher concentrations of oxygen and larger strains were associated with increased damage. In addition, other studies [39,40], by employing first principle density functional calculations, found that oxygen preferentially segregates at the γ/γ' ($Ni/Ni_3Al$) interface and results in a reduction of the cleavage energy (energy required to separate the crystal structure).

Since the temperature of 550°C investigated here is much lower than 1000°C, it is expected that the misfit strains are also lower, resulting in a lower number of dislocations at the γ/γ'interface. However, it is well established that at higher temperatures the damage mechanism of creep prevails [41,42], during which, the large negative misfits promote particle coalescence and the formation of rafts normal to the tensile loading direction that form a plate-like structure on the transverse face [43]. This microstructural change opposes glide of dislocations through the γ channels [44] and thus alters the concentration of dislocation defects around the previously cuboidal γ'. Therefore a form of dynamic

embrittlement, driven by a faster, short circuit diffusion of oxygen through dislocation defects along the γ/γ’ interface, might be more detrimental at intermediate temperatures.

The occasional shearing of the γ’ particles is generally observed to take place at an angle of approximately 45° to the loading axis, indicating that slip along the favourable {111} planes is not completely suppressed at these temperatures. This suggests that at 550°C a combination of planar slip damage and time dependent (oxidation) damage act simultaneously at the crack tip. Evidence of dislocations shearing the γ’ particles ahead of the crack tip (Figure 19) indicate that the deformation micro-mechanism is similar to that at room temperature, where dislocations glide in the γ matrix and shear the γ’ particles. Nevertheless, the crack tips shown in Figure 13 and the secondary cracks in Figure 16, were found to propagate predominantly nea r the γ/γ’ interface suggesting that oxidation influences propagation through a more macroscopic mechanism that could be explained by a form of dynamic embrittlement.

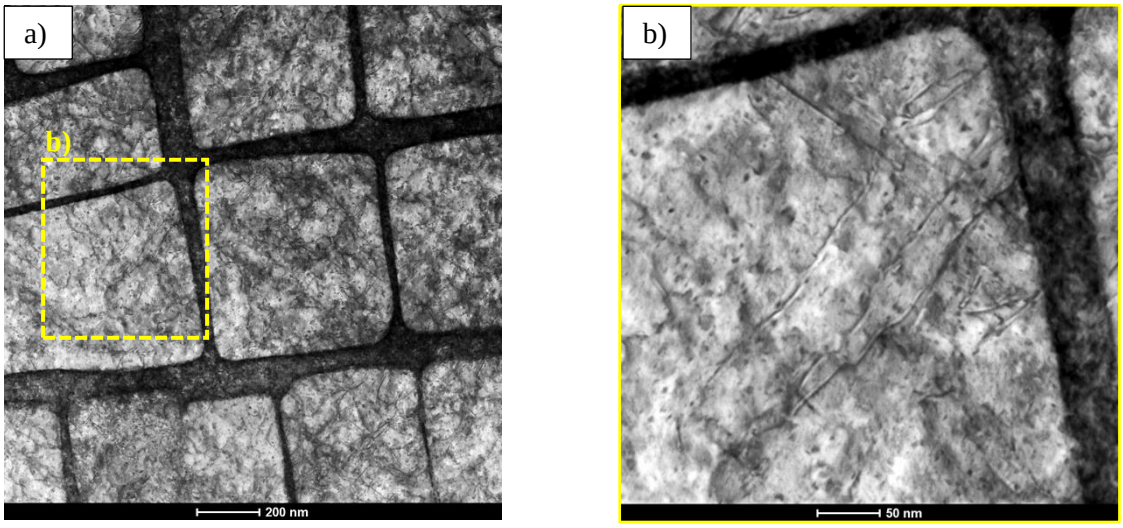


Figure 19: Dislocations propagating along a γ' particle located 3.5μm ahead of “crack tip 2”.

# 5 Conclusions

The effects of oxidation during dwell fatigue on the long crack propagation of CMSX-4 at 550°C were investigated and based on the aforementioned results and discussion, the following conclusions can be made:

1. The macroscopic fatigue crack propagation of CMSX-4 at 550°C in both air and vacuum occurred in the nominal growth direction producing a Stage II - like fracture surface. At 550°C in both air and vacuum the crack propagated along the γ/γ′ interface.
2. The FCP rate of CMSX-4 at 550°C is similar in air and vacuum. The fundamentally more rapid increased Stage I propagation in vacuum and the oxidation induced crack closure in air offset the overall effect of any oxidation induced damage mechanisms on crack growth rate.
3. Fatigue crack propagation with longer dwells results in rougher fracture surfaces indicating a more complex crack front. Examination of fatigue cracks that formed under sustained load for 12h (simulating a long dwell) had a complex morphology with multiple branches emanating from the main body forming a number of tips.
4. The crack propagation rates in single crystals are affected by the crack history particularly due to the formation of large facets. The fundamentally faster Stage I and the roughness induced closure results in less predictable FCP rates and significant sample to sample variability.
5. A layered oxide structure is formed at the crack tip of CMSX-4 during dwell fatigue at 550°C. This consists of an outer Co and Ni-rich oxide and an inner dominantly Al-rich oxide with Cr and Ti-rich oxides also being present. Even though this sequence is in good agreement with thermodynamic predictions, isothermal oxidation of unstressed samples did not form external Co-rich oxides indicating that the plastic strain acting at the crack tip alters the kinetics of the oxide species.
6. The micro-mechanism of fatigue crack propagation at intermediate temperatures is a complex process with several competing mechanisms acting on the crack tip simultaneously. Crystallographic slip damage by γ’ shearing is still active at these temperatures but at the same time thermally activated processes that promote propagation through the γ channels also take place. In addition, the effects of oxidation are two-fold. Even though the temperature is not high enough to cause embrittlement of a microstructural element ahead of the crack tip, finger-like protrusions of oxide were found to penetrate the material ahead of the crack tip. The kinetics of such a mechanism are accentuated by the plastic strains at the crack tip, which

given enough time can promote cleavage fracture at the γ/γ' interface. The rate of oxide formation on the crack tip surfaces is high enough to form thick oxides that bridge the CTO and reduce the effective driving force.

## 6 Acknowledgements

Thanks are due to the EPSRC (Grant 512444116) and Uniper Technologies for the funding support and Rugby Labs - GE Power (formerly Alstom) for materials supply. The authors also would like to thank Dr Geoff West and the WMG microscopy centre at Warwick University for access to the STEM-EDS and FIB facilities.

## Data Statement

All data supporting this study are openly available from the University of Southampton repository at http://doi.org/XXXXXXX

## 7 References

[1] M.P. Miller, D.L. McDowell, R.L.T. Oehmke, A Creep-Fatigue-Oxidation Microcrack Propagation Model for Thermomechanical Fatigue, J. Eng. Mater. Technol. 114 (1992) 282. doi:10.1115/1.2904174.

[2] M. Dedekind, L. Harris, Evaluation of premature failure of a gas turbine component, Int. J. Press. Vessel. Pip. 66 (1996) 59–76.

[3] J. Reuchet, L. Remy, Fatigue oxidation interaction in a superalloy—application to life prediction in high temperature low cycle fatigue, Metall. Trans. A. 14 (1983) 141–149. doi:10.1007/BF02643747.

[4] P.R. Wei, Z. Huang, Influence of dwell time on fatigue crack growth in nickel-base superalloys, Mater. Sci. Eng. A. 336 (2002) 209–214. doi:10.1016/S0921-5093(01)01957-8.

[5] M.R. Joyce, X. Wu, P. a. S. Reed, The effect of environment and orientation on fatigue crack growth behaviour of CMSX-4 nickel base single crystal at 650 °C, Mater. Lett. 58 (2004) 99–103. doi:10.1016/S0167-577X(03)00423-3.

[6] A. Defrense, L. Remy, Fatigue behaviour of CMSX 2 superalloy [001] single crystals at high temperature. I. Low cycle fatigue of notched specimens, Mater. Sci. Eng. A. A129 (1990) 45–53.

[7] E. Fleury, L. Rémy, Low cycle fatigue damage in nickel-base superalloy single crystals at elevated temperature, Mater. Sci. Eng. A. 167 (1993) 23–30. doi:10.1016/0921-5093(93)90332-9.

[8] L. Remy, A. Alam, N. Haddar, A. Koster, N. Marchal, Growth of small cracks and prediction of lifetime in high-temperature alloys, Mater. Sci. Eng. A. 468–470 (2007) 40–50. doi:10.1016/J.MSEA.2006.08.133.

[9] L. Rémy, M. Geuffrard, A. Alam, A. Köster, E. Fleury, Effects of microstructure in high temperature fatigue: Lifetime to crack initiation of a single crystal superalloy in high temperature low cycle fatigue, Int. J. Fatigue. 57 (2013) 37–49. doi:10.1016/j.ijfatigue.2012.10.013.

[10] P.J. Cotterill, J.E. King, Role of oxides in fatigue crack propagation, Mater. Sci. Technol. 6 (1990) 19–31.

[11] A. Shyam, W.W. Milligan, A model for slip irreversibility, and its effect on the fatigue crack propagation threshold in a nickel-base superalloy, Acta Mater. 53 (2005) 835–844. doi:10.1016/j.actamat.2004.10.036.

[12] M. Gell, D.J. Duquette, The Effects of Environment on the Elevated Temperature Fatigue Behavior of Nickel-Base Superalloy Single Crystals, Metall. Trans. 3 (1972).

[13] A. Sengupta, S.K. Putatunda, L. Bartosiewicz, J. Hangas, P.J. Nailos, M. Peputapeck, F.E. Alberts, Tensile behavior of a new single-crystal nickel-based superalloy (CMSX-4) at room

and elevated temperatures, J. Mater. Eng. Perform. 3 (1994) 73–81. doi:10.1007/BF02654502.

[14] D. Gustafsson, J.J. Moverare, S. Johansson, K. Simonsson, M. Hörnqvist, T. Månsson, S. Sjöström, Influence of high temperature hold times on the fatigue crack propagation in Inconel 718, Int. J. Fatigue. 33 (2011) 1461–1469. doi:10.1016/j.ijfatigue.2011.05.011.

[15] G.R. Leverant, M. Gell, The influence of temperature and cyclic frequency on the fatigue fracture of cube oriented nickel-base superalloy single crystals, Metall. Trans. A. 6 (1975) 367–371. doi:10.1007/BF02667291.

[16] P.A.S. Reed, Fatigue crack growth mechanisms in superalloys : overview, Mater. Sci. Technol. 25 (2009). doi:10.1179/174328408X361463.

[17] M.B. Henderson, J.W. Martin, Influence of precipitate morphology on the high temperature fatigue properties of SRR99, Acta Metall. Mater. 43 (1995) 4035–4043. doi:10.1016/0956-7151(95)00113-A.

[18] A. Sengupta, S.K. Putatunda, M. Balogh, Fatigue Crack Growth Behavior of a New Single Crystal Nickel-Based Superalloy ( CMSX-4 ) at 650C, (1994) 540–550.

[19] P.H. Thornton, R.G. Davies, T.L. Johnston, The temperature dependence of the flow stress of the γ′ phase based upon Ni3Al, Metall. Trans. 1 (1970) 207–218. doi:10.1007/BF02819263.

[20] P. Neumann, Coarse slip model of fatigue, Acta Metall. 17 (1969) 1219–1225. doi:10.1016/0001-6160(69)90099-6.

[21] P.A.S. Reed, I. Sinclair, X.D. Wu, Fatigue crack path prediction in UDIMET 720 nickel-based alloy single crystals, Metall. Mater. Trans. A. 31 (2000) 109–123. doi:10.1007/s11661-000-0058-6.

[22] P.K. Wright, M. Jain, D. Cameron, High Cycle Fatigue in Single Crystal Superalloy: Time dependence at Elevated Temperatures, Superalloys. 666 (2004).

[23] J. Tong, J. Byrne, Effects of frequency on fatigue crack growth at elevated temperature,

Fatigue Fract. Eng. Mater. Struct. 22 (1999) 185–193. doi:10.1046/j.1460-2695.1999.00160.x.

[24] T. Weerasooriya, Effect of frequency on fatigue crack growth rate of Inconel 718 at high temperatures, Dayton, Ohio, 1987.

[25] R. Jiang, D.J. Bull, D. Proprentner, B. Shollock, P.A.S. Reed, Effects of oxygen-related damage on dwell-fatigue crack propagation in a P/M Ni-based superalloy: From 2D to 3D assessment, Int. J. Fatigue. 99 (2017) 175–186. doi:10.1016/j.ijfatigue.2017.03.003.

[26] X.-K. Zhu, J.A. Joyce, Review of fracture toughness (G, K, J, CTOD, CTOA) testing and standardization, Eng. Fract. Mech. 85 (2012) 1–46. doi:10.1016/j.engfracmech.2012.02.001.

[27] A. Evangelou, K. Soady, S. Lockyer, N. Gao, P.A.S. Reed, Oxidation behaviour of single crystal nickel-based superalloys: intermediate temperature effects at 450–550°C, Mater. Sci. Technol. (2018) 1–14.

[28] R. Jiang, P.A.S. Reed, Critical assessment: oxygen-assisted fatigue crack propagation in turbine disc superalloys, Mater. Sci. Technol. 32 (2016) 401–406. doi:10.1080/02670836.2016.1148227.

[29] C.K. Sudbrack, S.L. Draper, T.T. Gorman, J. Telesman, T.P. Gabb, D.R. Hull, Oxidation and the effects of high temperature exposures on notched fatigue life of an advanced powder metallurgy disk superalloy, Superalloys 2012. (2012) 863–872.

[30] Y. Kiyak, B. Fedelich, T. May, A. Pfennig, Simulation of crack growth under low cycle fatigue at high temperature in a single crystal superalloy, Eng. Fract. Mech. 75 (2008) 2418–2443. doi:10.1016/j.engfracmech.2007.08.002.

[31] J.M. Martínez-Esnaola, A. Martín-Meizoso, E.E. Affeldt, A. Bennett, M. Fuentes, High temperature fatigue in single crystal superalloys, Fatigue Fract. Eng. Mater. Struct. 20 (1997) 771–788.

[32] J.L. Bouvard, F. Gallerneau, P. Paulmier, J.L. Chaboche, A phenomenological model to predict the crack growth in single crystal superalloys at high temperature, Int. J. Fatigue. 38

(2012) 130–143. doi:10.1016/j.ijfatigue.2011.12.011.

[33] J.L. Bouvard, J.L. Chaboche, F. Feyel, F. Gallerneau, A cohesive zone model for fatigue and creep–fatigue crack growth in single crystal superalloys, Int. J. Fatigue. 31 (2009) 868–879. doi:10.1016/j.ijfatigue.2008.11.002.

[34] H. Long, H. Wei, Y. Liu, S. Mao, J. Zhang, S. Xiang, Y. Chen, W. Gui, Q. Li, Z. Zhang, X. Han, Effect of lattice misfit on the evolution of the dislocation structure in Ni-based single crystal superalloys during thermal exposure, Acta Mater. 120 (2016) 95–107. doi:10.1016/j.actamat.2016.08.035.

[35] A. Ma, D. Dye, R.C. Reed, A model for the creep deformation behaviour of single-crystal superalloy CMSX-4, Acta Mater. 56 (2008) 1657–1670. doi:10.1016/j.actamat.2007.11.031.

[36] G. Brunetti, A. Settefrati, A. Hazotte, S. Denis, J.-J. Fundenberger, A. Tidu, E. Bouzy, Determination of γ-γ' lattice misfit in a single-crystal nickel-based superalloy using convergent beam electron diffraction aided by finite element calculations, Micron. 43 (2012) 396–406. doi:10.1016/j.micron.2011.10.009.

[37] J.X. Zhang, J.C. Wang, H. Harada, Y. Koizumi, The effect of lattice misfit on the dislocation motion in superalloys during high-temperature low-stress creep, (2005). doi:10.1016/j.actamat.2005.06.013.

[38] A. Karabela, L.G. Zhao, B. Lin, J. Tong, M.C. Hardy, Oxygen diffusion and crack growth for a nickel-based superalloy under fatigue-oxidation conditions, Mater. Sci. Eng. A. 567 (2013) 46–57. doi:10.1016/j.msea.2012.12.088.

[39] S. Sanyal, U. V Waghmare, T. Hanlon, E.L. Hall, P. Subramanian, M.F.X. Gigliotti, Interfaces in Ni-based Superalloys and Implications for Mechanical Behavior and Environmental Embrittlement: A First-principles Study, (2012).

[40] S. Sanyal, U. V. Waghmare, P.R. Subramanian, M.F.X. Gigliotti, First-principles understanding of environmental embrittlement of the Ni/Ni3Al interface, Scr. Mater. 63 (2010)

391–394. doi:10.1016/j.scriptamat.2010.04.033.

[41] D.W. Maclachlan, D.M. Knowles, Creep-Behavior Modeling of the Single-Crystal Superalloy CMSX-4, Metall. Mater. Trans. A. 31A (2000).

[42] C.M.F. Rae, M.A. Rist, D.C. Cox, R.C. Reed, N. Matan, On the primary creep of CMSX-4 superalloy single crystals, Metall. Mater. Trans. A. 31 (2000) 2219–2228. doi:10.1007/s11661-000-0139-6.

[43] F.R.N. Nabarro, Rafting in Superalloys, Metall. Mater. Trans. A. 27A (1996).

[44] R.. Reed, N. Matan, D.. Cox, M.. Rist, C.M.. Rae, Creep of CMSX-4 superalloy single crystals: effects of rafting at high temperature, Acta Mater. 47 (1999) 3367–3381. doi:10.1016/S1359-6454(99)00217-7.